MAGNETOHYDRODYNAMICS Vol. 41 (2005), No. 1, pp. 39–51

ELECTRO-VORTEX FLOWS IN A SQUARE LAYER OF LIQUID METAL

I. Kolesnichenko[1], *S. Khripchenko*[1], *D. Buchenau*[2], *G. Gerbeth*[2]

[1] *Institute of Continuous Media Mechanics, Perm, Russia*
[2] *Forschungszentrum Rossendorf, Dresden, Germany*

We study electro-vortex flows generated by electro-magnetic forces in a shallow square layer of liquid metal. The force driving the flow is produced by the interaction between the electric current flowing through the layer and its own magnetic field. Rotational parts of that force are particularly caused by ferromagnetic yokes placed around the layer. Depending of the position and type of those yokes flows of one-, two- or four-eddies are initiated. The basic flow structure and the related velocity oscillations have been investigated both by experimental techniques using the ultrasound Doppler velocimetry and by numerical calculations. Compared to the single vortex flow the double vortex flow shows a much higher level of large-scale velocity oscillations. The theoretical model turned out to be in good agreement with the experimental data.

Introduction. The object of the present study is a vortex flow in a thin layer of conducting fluid generated by an electro-magnetic (EM) force. In many cases of Magnetohydrodynamics (MHD) such EM forces result from the interaction of the fluid flow with an external magnetic field or by induction due to the time variation of an external magnetic field. In the present paper we consider a special version of EM forces, namely, the interaction of an externally applied electrical current with its own magnetic field. Of particular interest in this context is the tailoring of the EM forces by the use of external ferromagnetic yokes which modify the magnetic field distribution and, typically, cause a non-conservative, thus flow-driving EM force distribution.

We study this flow-driving action by considering a simple flat channel as shown in Figs. 1 and 2. The layer *1* (Fig. 1) has the form of a rectangular parallelepiped,

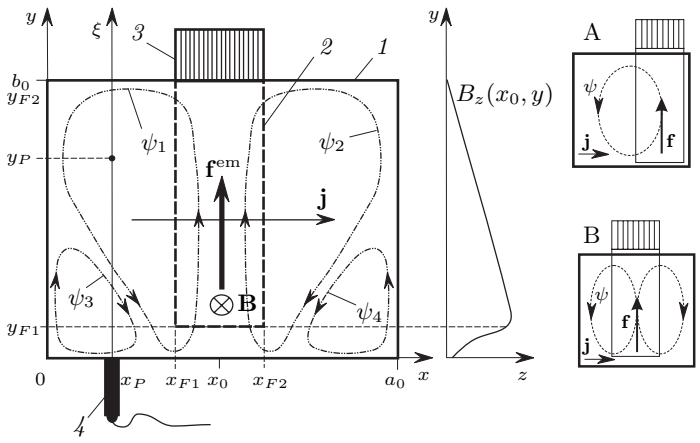

Fig. 1. Left – sketch of the MHD layer (top view), center – induction profile, right – schemes of EVF depending on position of the C-core *2* (types A and B).

the thickness d_0 of which is much less than its sizes a_0 and b_0 in the horizontal plane. A direct electrical current I_0 with the uniform density $\mathbf{j} = (j_x, 0, 0)$, where $j_x = I_0/b_0 d_0$, flows through the fluid layer between vertical walls. Its own magnetic field with the induction $\mathbf{B}$ is enhanced by ferromagnetic yokes *2* with jumper *3*. Since the vertical component of the induction vector is much larger than the horizontal one we set $\mathbf{B}(x, y) = (0, 0, B_z(x, y))$. The electro-magnetic force $\mathbf{f}^{\text{em}} = (0, -j_x B_z, 0)$ is rotational due to the restriction of the yoke sizes in the plane and, therefore, generates an electro-vortex flow (EVF) in the layer. The type of the EVF depends on the position of yoke *2*. Thus, if the yoke has a jumper (which is a "C-core") an EVF with one (type A) or two (type B) primary eddies can be initiated. In addition, the generated flows may be unstable.

In the context of the formulated problem it has been found that the EVF of A and B type with a free surface looses stability, which results in oscillations of eddies [1]. Certainly, oscillations of the free surface interact with the EVF, but it seems to be not the main reason of instability since in similar vortex flows such oscillations may occur even in a layer without a free surface [2]. In case of a layer with free surface, the EVF can be easily investigated experimentally. When employing gallium alloys, it is sufficient to apply a thin layer of water solution of hydrochloric acid over the surface of a liquid metal. Small bubbles of hydrogen generated on the surface in the course of chemical reactions play the role of tracers allowing us to detect the appearance of any flow modes. Using this method, the two-eddies EVF has been studied and compared with numerical simulations [3].

In the present work, we investigate the stationary state and oscillations of the EVF in a layer without a free surface by experimental and numerical methods. In experiment we have employed the Ultrasound Doppler Velocimetry (UDV). With this non-invasive technique we can obtain profiles of the velocity component along the ultrasonic beam and gain detailed information about the EVF, which can be readily processed and compared with numerical results. For the theoretical part we made use of the mathematical model formulated in [4], where it was applied for the investigation of the processes in a technological device based on such an MHD-layer. The model is based on some simplification reducing the problem complexity. Of course, the validity of this approach needs to be checked by comparing the theoretical results for the structure of the velocity field with the corresponding experimental data. In [4] the results obtained by the model were tested using the integral experimental characteristics only. The present study provides for the first time a detailed comparison with measured velocity profiles. In that way it delivers enough evidence supporting the correctness of the calculations and, thus, extends the capabilities of the theoretical approach to allow for reliable predictions in working with different devices based on such MHD layers.

1. Experimental setup. We studied the EVF in a plane quadratic layer *1* (Fig. 2) of liquid metal (gallium alloy: 20.5% In+67% Ga+12.5% Sn) with the thickness $d_0 = 0.01\,\text{m}$ and sizes $a_0 = b_0 = 0.1\,\text{m}$. The gallium alloy had the following properties: $\rho = 6256\,\text{kg/m}^3$ – density, $\nu = 3.1 \cdot 10^{-7}\,\text{m}^2/\text{s}$ – kinematic viscosity, $\sigma = 3.56 \cdot 10^6\,\text{S/m}$ – electrical conductivity. The layer was bounded by vertical walls: one pair of opposite walls *5* was made of copper and played the role of electrodes, another pair of opposite walls *6* was made of plexiglass as well as the bottom *7* and the lid *8* (not shown in Fig. 2). Owing to the lid *8* with a rubber seal, the layer was enclosed completely in the solid cavity. The direct electrical current source providing currents in the range of $I_0 = 0 \div 1100\,\text{A}$ was connected through feed wires to electrodes *5*. The use of the ferromagnetic yokes *2* ensures variation of the magnetic field of the electrical current increasing the

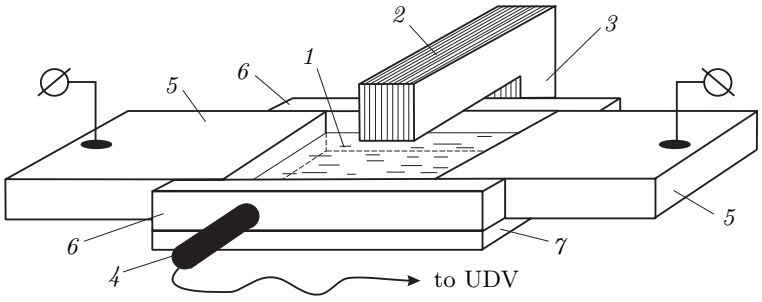

Fig. 2. Scheme of experimental setup without lid.

value of the field in the gap of $\delta = 0.03\,\mathrm{m}$ between the yokes. The yokes had the sizes $a_F = x_{F2} - x_{F1} = 0.03\,\mathrm{m}$, $b_F = y_{F2} - y_{F1} = 0.15\,\mathrm{m}$ (see Fig. 1) and the jumper *3*. The use of this "C-core" allowed a generation of the EVF with one or two primary eddies. Moving the C-core (changing the value y_{F2} form 0 up to 0.1 m) we could increase the intensity of the EVF. The maximal local value of the magnetic field $B_0 = I_0\mu_0/\delta = 0.044\,\mathrm{T}$ was achieved at the C-core position $y_{F2} = 0$ for the current $I_0 = 1100\,\mathrm{A}$ (where $\mu_0 = 4\pi \cdot 10^{-7}\,\mathrm{H/m}$ – vacuum permeability).

To measure the velocity field we employed the UDV "DOP2000" manufactured by Signal Processing SA (Lausanne, Switzerland). This device operates on the principle of the sound wave reflection from scattering particles moving with the flow. Measuring the time delay between the emitted and received signals and the frequency shift caused by the Doppler effect, we can find the location and velocity of the particle. The UDV consists of the control device, which serves to process signals and to obtain the velocity profiles, and the transducer *4* (see Figs. 1, 2) connected to a control device. The transducer generates the pulsing ultrasound (US) beam and receives the echo reflected from the particles. By making measurements with different transducers, we came to the conclusion that the focused 4 MHz transducer of 8 mm diameter (TR30405, Signal Processing, Lausanne, Switzerland) is best suited for investigations of this kind. The sound velocity in the gallium alloy was $V^{\mathrm{sound}} = 2740\,\mathrm{m/s}$, the wavelength $\lambda = 0.7\,\mathrm{mm}$ and the spatial resolution along the beam was 5.7 mm. In several works concerning the application of UDV, the transducer was placed not normally to the rectangular [5] or cylindrical [6, 7] walls ensuring an angle between the mainstream velocity and the US beam, which was necessary to derive the velocity profile. In our study we directed the US beam normally to the walls *6* as this direction provided directly the spanwise velocity component. As a material for the walls *6* we chose plexiglass, because the contact region between this material and gallium alloy has a small acoustic impedance. Grease placed between the transducer *4* and the wall *6* ensured a good acoustic contact.

Using the gallium alloy for our study, we faced the problem of measurements in an intense EVF with a high level of noise, although the UDV is able to measure rather high velocities. Using vacuum degassing and frequent cleaning of the gallium alloy, we have solved this problem. There are two main kinds of oxides in gallium alloy: GaO_2 (density $4.77 \cdot 10^3\,\mathrm{kg/m^3}$) and Ga_2O_3 (density $6.44 \cdot 10^3\,\mathrm{kg/m^3}$) [6]. These oxides played the role of particles ensuring a good level of scattering signals, but sometimes during experiment there occurred a necessity of mixing the oxides with the gallium alloy using an intensive EVF.

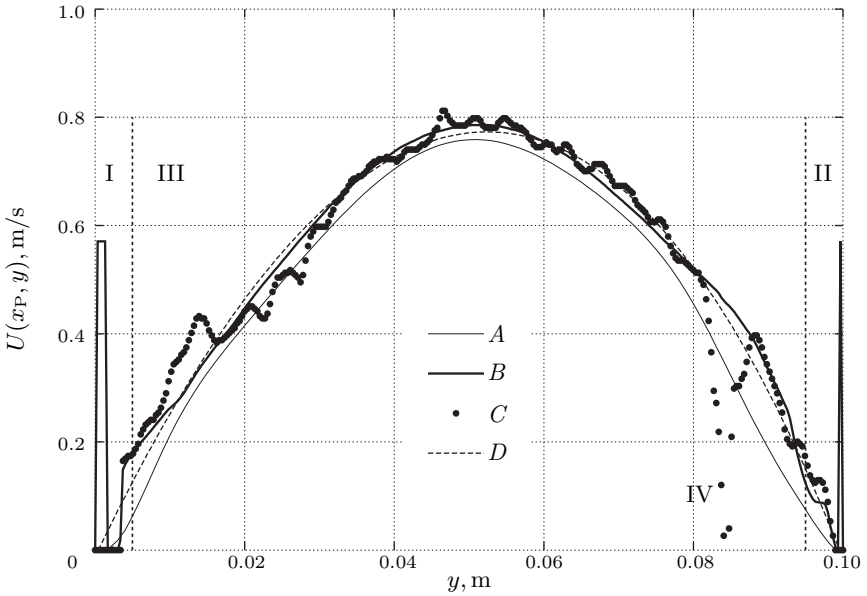

Fig. 3. Example of velocity profiles ($I_0 = 1000$ A, type A): A – calculated profile $V_y(x_\mathrm{P}, y, t^*)$, B – mean of $N_t = 512$ experimental profiles $\overline{U}(x_\mathrm{P}, y)$, C – instantaneous experimental profile $U(x_\mathrm{P}, y, t^*)$, D – approximation of U by Chebyshev polynomials (U^appr).

During each UDV measurement we obtained a sequence of N^pr velocity profiles $U(x_\mathrm{P}, y^\mathrm{pr}, t^\mathrm{pr})$ along the axis ξ (Fig. 1). Here x_P is the position of the US transducer *4* (we used $x_\mathrm{P} = \{5; 10; ..90; 95\}$ mm), y^pr is the vector of N_y points along ξ (we used $N_y = 304$), t^pr is the vector of N_t points on the time axis (we used $N_t = \{512; 1024; 4096\}$). Figure 3 shows one of the profiles from the obtained sequence at some fixed time moment t^*. Due to multiple reflections, the profile in the regions near the walls I and II is non-obtainable (but actually, the value at the bottom has to be zero because of the "non-leakage" condition). We took into account the "shadow" effect caused by local losses of the signal (IV on Fig. 3) by making use of a "rejecting zero" procedure.

2. Mathematical model. To formulate the mathematical model describing the electro-vortex flow of laminar and turbulent nature observed during experiments, we have used a system of MHD-equations resulting from a suitable reduction of the problem complexity. The model uses the following scale parameters to make the related equations non-dimensional: d_0, ν/d_0, $d_0^2\nu$, $\rho\nu^2/d_0^2$, I_0/d_0^2, $B_0 = I_0\mu_0/\delta$ for length, velocity, time, pressure, electrical current density and magnetic induction, respectively. At first, we made use of a low magnetic Reynolds number assumption $\mathrm{Rm} \ll \delta/a_0$ [8]. With this approximation, one can ignore the influence of the flow on the electro-magnetic field. In our case, $\mathrm{Rm} = \mu_0\sigma V_0 d_0 = 0.044 V_0$ and $\delta/a_0 = 0.3$, so that this approach was appropriate for our treatment up to a maximal velocity of $V_0 < 1$ m/s. As the results have shown, the same case was in our experiments. Therefore, we could calculate the electro-magnetic force $\mathbf{f}^\mathrm{em}$ using only the electrical current j_x and the induction B_z, which can be found by the method described in [1].

Another approximation which can be applied to thin layers $d_0 \ll \min(a_0, b_0)$, is based on the assumption that the velocity field vector has no vertical com-

ponent. We approximated the horizontal velocity components $V_i^{3D}(x,y,z,t) = V_i(x,y,t)f_V(z,\mathrm{Ha},\mathrm{Re})$ by multiplying the planar velocities V_i with a function f_V which describes the vertical profiles [9] ($i = 1,2$ with the notation $V_1 \equiv V_x$; $V_2 \equiv V_y$). In addition, an integration of the equations along the vertical axis throughout the layer [9] is used. The local profile function $f_V(z,\mathrm{Ha},\mathrm{Re})$ depends on the local Reynolds number $\mathrm{Re} = V_i$ and the Hartmann number $\mathrm{Ha} = B_0 B_z d_0 \sqrt{\sigma/\rho\nu}$, and it is normalized as $\int_0^1 f_V(z,\mathrm{Ha},\mathrm{Re})\mathrm{d}z = 1$. In our case these numbers have the following maximum values: $\mathrm{Re} \le 3.3 \cdot 10^4$, $\mathrm{Ha} \le 34$. It means that the flow may be turbulent, and the magnetic field may influence the flow structure and the instability threshold. As it will be shown later, this profile function is used to describe the main part of the turbulent dissipation caused by friction near the top and bottom walls where the vertical gradients of the horizontal velocity components $\partial_z V_i$ ($i,j = \overline{1,2}$) are very high. The remaining part of turbulent dissipation, characterized by the horizontal gradients of the horizontal velocity components $\partial_j V_i$ ($i,j = \overline{1,2}$), was described in terms of the k^{t}–ω^{t} model involving a turbulent viscosity. Eventually, the Navie–Stokes equation, integrated along the vertical axis through the layer, is written as

$$\frac{\partial V_i}{\partial t} + V_j \frac{\partial V_i}{\partial x_j} = -\frac{\partial (P + k^{\mathrm{t}})}{\partial x_i} + \nu^{\mathrm{t}} \frac{\partial^2 V_i}{\partial x_j^2} + \kappa V_i + \frac{\partial \nu^{\mathrm{t}}}{\partial x_j} e_{ij} + S f_i^{\mathrm{em}} \quad (i,j = \overline{1,2}), \quad (1)$$

or in a vorticity ($\omega = \partial_y V_x - \partial_x V_y$) streamfunction formulation as

$$\frac{\partial \omega}{\partial t} + \frac{\partial (V_x \omega)}{\partial x} + \frac{\partial (V_y \omega)}{\partial y} = \left(\frac{\partial^2 \psi}{\partial x^2} \frac{\partial^2 \nu^{\mathrm{t}}}{\partial y^2} + \frac{\partial^2 \psi}{\partial y^2} \frac{\partial^2 \nu^{\mathrm{t}}}{\partial x^2} - 2 \frac{\partial^2 \psi}{\partial x \partial y} \frac{\partial^2 \nu^{\mathrm{t}}}{\partial x \partial y} \right) +$$
$$+ \triangle(\nu^{\mathrm{t}} \omega) + \left(\frac{\partial (V_x \kappa)}{\partial y} - \frac{\partial (V_y \kappa)}{\partial x} \right) + S \left(\frac{\partial f_x^{\mathrm{em}}}{\partial y} - \frac{\partial f_y^{\mathrm{em}}}{\partial x} \right). \quad (2)$$

Here we use the following notations: P is the pressure, k^{t} is the turbulent kinetic energy, $\nu^{\mathrm{t}} = (1 + \eta^{\mathrm{t}}/\rho\nu)$ is the turbulent kinematic viscosity, κ is the factor describing the turbulent friction near the horizontal solid walls, $e_{ij} = V_{i,j} + V_{j,i}$ is the tensor of velocity deformation, and $S = I_0^2 \mu_0 d_0 / \rho \nu^2 \delta$ is the parameter of MHD interaction. The relations between the velocity, stream function and vorticity are given as $\triangle\psi = \omega$, $V_x = \partial_y \psi$, $V_y = -\partial_x \psi$. At the solid side walls of the layer the no-slip condition for the velocity must be fulfilled: $V_i(x = \{0; a_0\}, y) = 0$, $V_i(x, y = \{0; b_0\}) = 0$.

The quantity κ appears after integrating the 3D Navier–Stokes equation. It is a field defined by the tangents to the velocity profile at the bottom and cover walls, or might be expressed as $\kappa(x,y,t) = 2\partial_z f_V(z,\mathrm{Ha},\mathrm{Re})|_{z=0}$ due to the symmetry of the profile. In our previous study [4], we defined κ using the linear model $\kappa = \kappa_1 + \kappa_2 |\mathbf{V}|$ obtained experimentally in [10] not taking into account the influence of the magnetic field on turbulence. In the present work, we have defined κ from known experimentally obtained relations [11] for the following types of flows of a conducting liquid in a flat channel in the absence and presence of a transverse magnetic field: laminar Poiseuille and Hartmann flows, laminar and turbulent Blasius and Hartmann boundary layer flows. Furthermore the hydraulic resistance coefficients λ_{hd}, revealed in work [11] are related to the gradient of velocity on the wall by the following equation

$$\partial_z V_i^{3D}|_{z=0} = \lambda_{\mathrm{hd}} \frac{\mathrm{Re}}{2}.$$

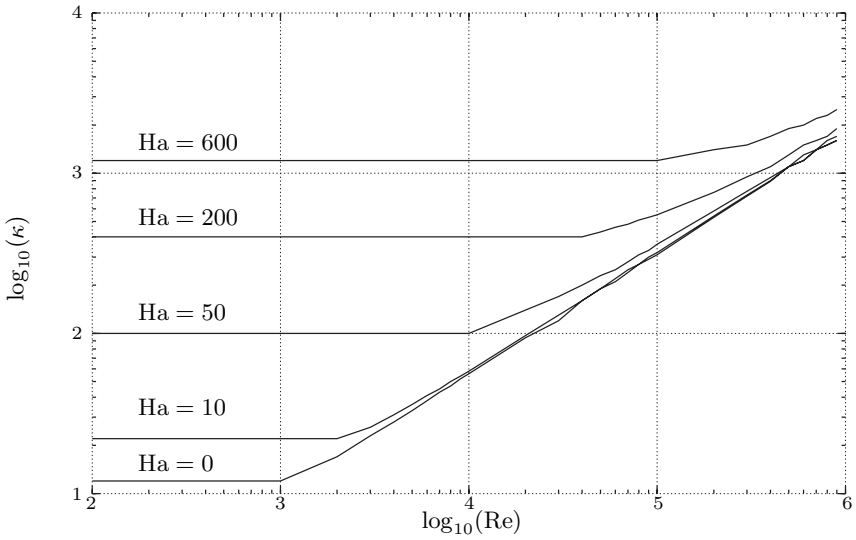

Fig. 4. Friction factor κ vs Reynolds and Hartmann numbers

Therefore the local friction factor $\kappa = \lambda_{\rm hd}{\rm Re}$ is defined in our model as follows:

$$\kappa = \begin{cases} 2\lambda_l {\rm Re}, & {\rm Re} < {\rm Re}^{\rm cr},\ {\rm Ha} < 4; \\ \lambda_h {\rm Re}, & {\rm Re} < {\rm Re}^{\rm cr},\ {\rm Ha} \geq 4; \\ \lambda_b {\rm Re}, & {\rm Re} \geq {\rm Re}^{\rm cr}; \end{cases} \tag{3}$$

$$\begin{gathered} {\rm Re}^{\rm cr} = 1280 \text{ (for Ha} < 5.95), \quad {\rm Re}^{\rm cr} = 215{\rm Ha} \text{ (for Ha} \geq 5.95); \\ \lambda_l = \frac{6}{\rm Re}, \quad \lambda_0 = 0.056{\rm Re}^{-1/4}, \quad \lambda_h({\rm Re}, {\rm Ha}) = \frac{2{\rm Ha}^2 \tanh({\rm Ha})}{{\rm Re}({\rm Ha} - \tanh({\rm Ha}))}; \\ \lambda_b = \lambda_h + (\lambda_0 - \lambda_l)\left(\frac{\lambda_h - \lambda_h^{\rm cr}}{\lambda_l - \lambda_h^{\rm cr}}\right)^{1+(1-{\rm Re}^{\rm cr}/{\rm Re})^2}, \quad \lambda_h^{\rm cr} = \lambda_h({\rm Re}^{\rm cr}, {\rm Ha}). \end{gathered}$$

Figure 4 shows the dependence of κ on Re calculated from (3) for several values of Ha.

As it was mentioned above, we apply a $k^{\rm t}$–$\omega^{\rm t}$ model [12] to take into account the part of dissipation due to the turbulence characterized by the horizontal gradients of the horizontal velocity components. With this model, we can find the turbulent viscosity $\nu^{\rm t} = k^{\rm t}/\omega^{\rm t}$ from the system of equations for the turbulent kinetic energy $k^{\rm t}$ and the specific dissipation rate $\omega^{\rm t}$ (which is the turbulent dissipation divided by the turbulent kinetic energy $\omega^{\rm t} = \epsilon^{\rm t}/k^{\rm t}$)

$$\frac{\partial k^{\rm t}}{\partial t} + V_j \frac{\partial k^{\rm t}}{\partial x_j} = -2(V_{i,j} + V_{j,i})V_{i,j}\nu^{\rm t} - \alpha_1 k^{\rm t}\omega + \frac{\partial}{\partial x_j}\left((1 + \alpha_2\nu^{\rm t})\frac{\partial k^{\rm t}}{\partial x_j}\right) \tag{4}$$

$$\frac{\partial \omega^{\rm t}}{\partial t} + V_j \frac{\partial \omega^{\rm t}}{\partial x_j} = \alpha_3(V_{i,j} + V_{j,i})V_{i,j}\nu^{\rm t} - \alpha_4(\omega^{\rm t})^2 + \frac{\partial}{\partial x_j}\left((1 + \alpha_2\nu^{\rm t})\frac{\partial \omega^{\rm t}}{\partial x_j}\right) \tag{5}$$

Here we use the coefficients $\alpha_1 = 0.09$, $\alpha_2 = 0.5$, $\alpha_3 = 0.05$, $\alpha_4 = 0.075$. On the solid side boundaries of the layer, the values of $k^{\rm t}$ and $\omega^{\rm t}$ are calculated using the turbulent logarithmic profile, characterized by the rate of the wall shear stress V_τ: $k^{\rm t} = V_\tau^2$, $\omega^{\rm t} = \sqrt{k^{\rm t}}/k_C\zeta$, where $k_C = 0.41$ is the Karman's constant and ζ is the wall distance.

3. Results and discussion. To analyse the experimentally and numerically obtained results, we have processed three types of information about the velocity fields: the values of the velocity component at the selected point $U(x_{\rm P}, y_{\rm P}, t)$ (see Fig. 1), the velocity profiles $U(x_{\rm P}, y_i, t)$ along the y-axis, and the time-averaged velocity fields represented by the stream-function $\overline{\psi}(x_j, y_i)$ (from here on the overscribed bar denotes the time-averaging procedure).

To process the experimentally obtained velocity profiles $U(x_{\rm P}, y_i, t)$, we have applied their approximation $U_M^{\rm appr}(x_{\rm P}, y_i, t)$ using the so-called shifted Chebyshev polynomials as the basis functions $T_M(\alpha) = \cos(p \cdot \arccos(2\alpha - 1))$ [13], where M is the degree of polynomials and α is the coordinate value from the range $[0, 1]$. These polynomials are orthogonal in the range $[0, 1]$ and form a complete and linear-independent system. The convergence of series expansions in these polynomials $U_M^{\rm appr}(x_{\rm P}, y_i, t) = \sum_{m=0}^{M} A_m(t) T_m(\alpha)$ is quite good for a selection of collocation points $\alpha_i = \cos(\pi y_i^*)/2 + 1/2$, $i = 0...N_y$, where $y_i^* = (y_i - y_{\min})/(y_{\max} - y_{\min})$. The shapes of the polynomial functions allow a close approximation of the boundary layers near the walls satisfying the no-slip condition. The motivation for the described Chebyshev approximation of the measured profiles is to separate the stationary velocity field from low-frequency oscillations. Using directly the measured velocity signals may lead to ambiguous results due to the roughness of the signals and the occurrence of losses in the measured profiles. Figure 3 illustrates a approximated velocity profile and a numerically calculated profile. It is seen that they are in good agreement. In our case the velocity profiles are rather smooth and, therefore, five basic functions were typically sufficient for a good approximation.

Figure 5 shows the dependence of the mean velocity $\overline{U}(x_{\rm P}, y_{\rm P})$ on the electrical current. It is seen that the larger the scale of eddies, the higher the velocity. As it could be expected from Eq. (1), the maximum mean velocities increase linearly with the external current. Note that for the range of Reynolds numbers considered here the resulting velocity typically scales with the square-root of the driving force. Figure 6 show the basic mean flow structures at a rather low value of the external

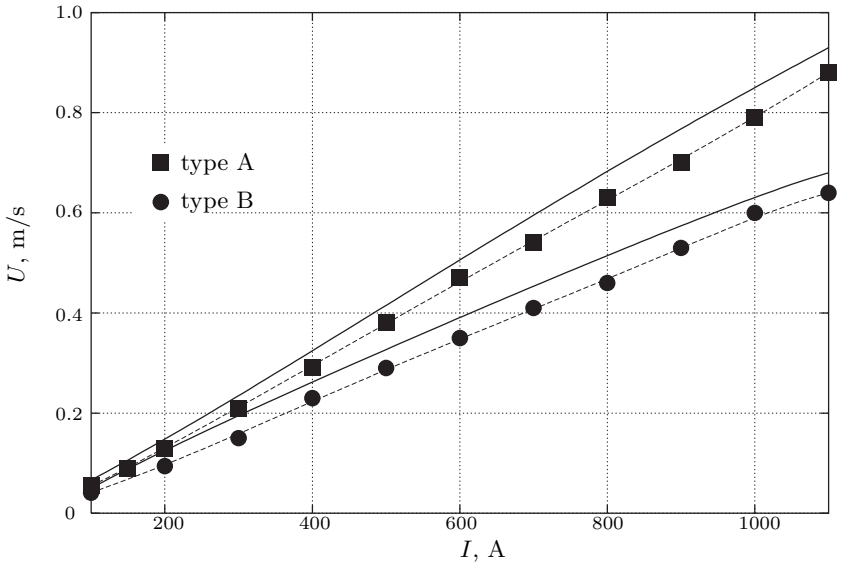

Fig. 5. Maximum mean velocity vs electrical current (here and after ■ – for the EVF of type A, ▲ – for the EVF of type B, solid lines – calculations).

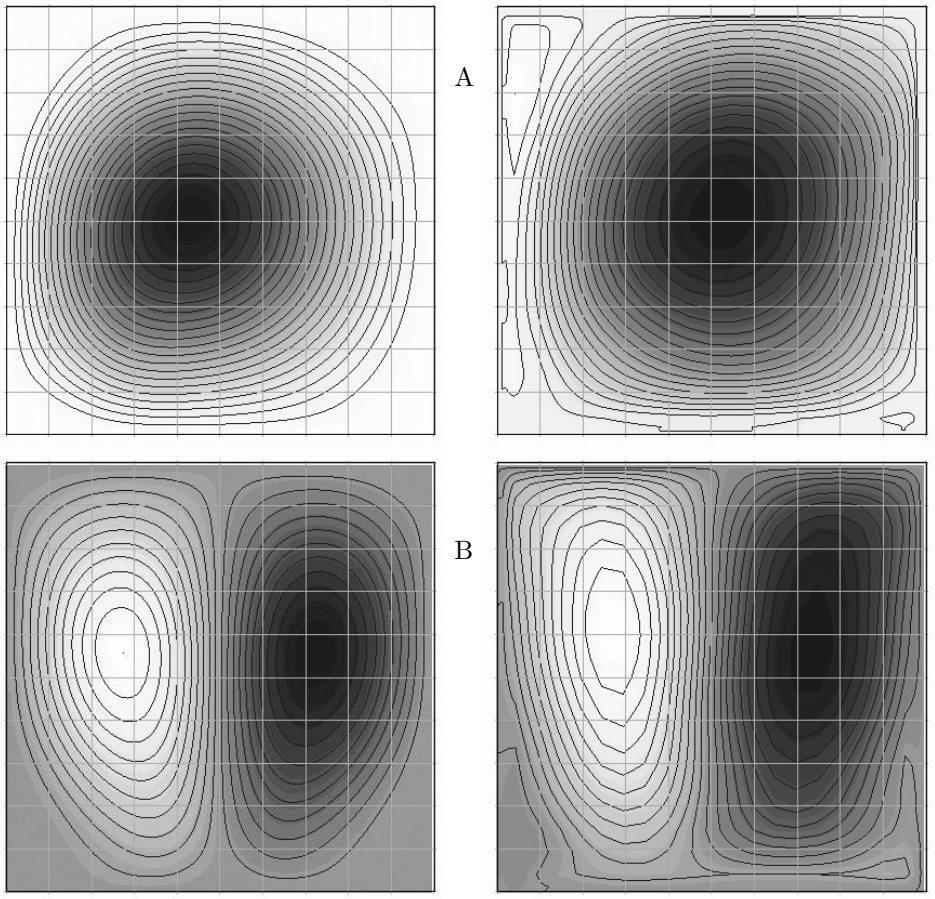

Fig. 6. Stream-function ψ for the EVF of types A and B (left – calculations, right – experiment).

current of $I_0 = 100\,\mathrm{A}$. The flows are sufficiently stable at this low current value and correspond to the the single- and double-vortex structure as sketched already in Fig. 2. Note that we do not explicitly address the problem of the basic laminar flows instability, which occurs in the range of $I_0 = (50 \pm 10)\,\mathrm{A}$, since the UDV measuring technique faces some limitations at lower fluid velocities [14].

A good agreement is seen between the experimental and theoretical results in Fig. 6. The experimental stream-functions have been obtained from the measured profiles in the following way. We measured a set of velocity profiles for the values of $x_p = j \times 5\,\mathrm{mm}$ ($j = 1...19$) by moving the UDV sensor along the side-wall of the layer. To construct the stream-function from those data, we calculated the Chebyshev approximation $\overline{U}_M^{\mathrm{appr}}(x_\mathrm{P}, y_i)$ of these profiles and integrated them along the x-axis (forward and backward averaging of the results of integration along the x-axis) according to

$$\psi(x_j, y_i) = 0.005 \left(\sum_{k=0}^{j} U_M^{\mathrm{appr}}(x_k, y_i) - \sum_{k=j}^{20} U_M^{\mathrm{appr}}(x_k, y_i) \right) /2. \qquad (6)$$

At the layer walls the stream-function is set to zero.

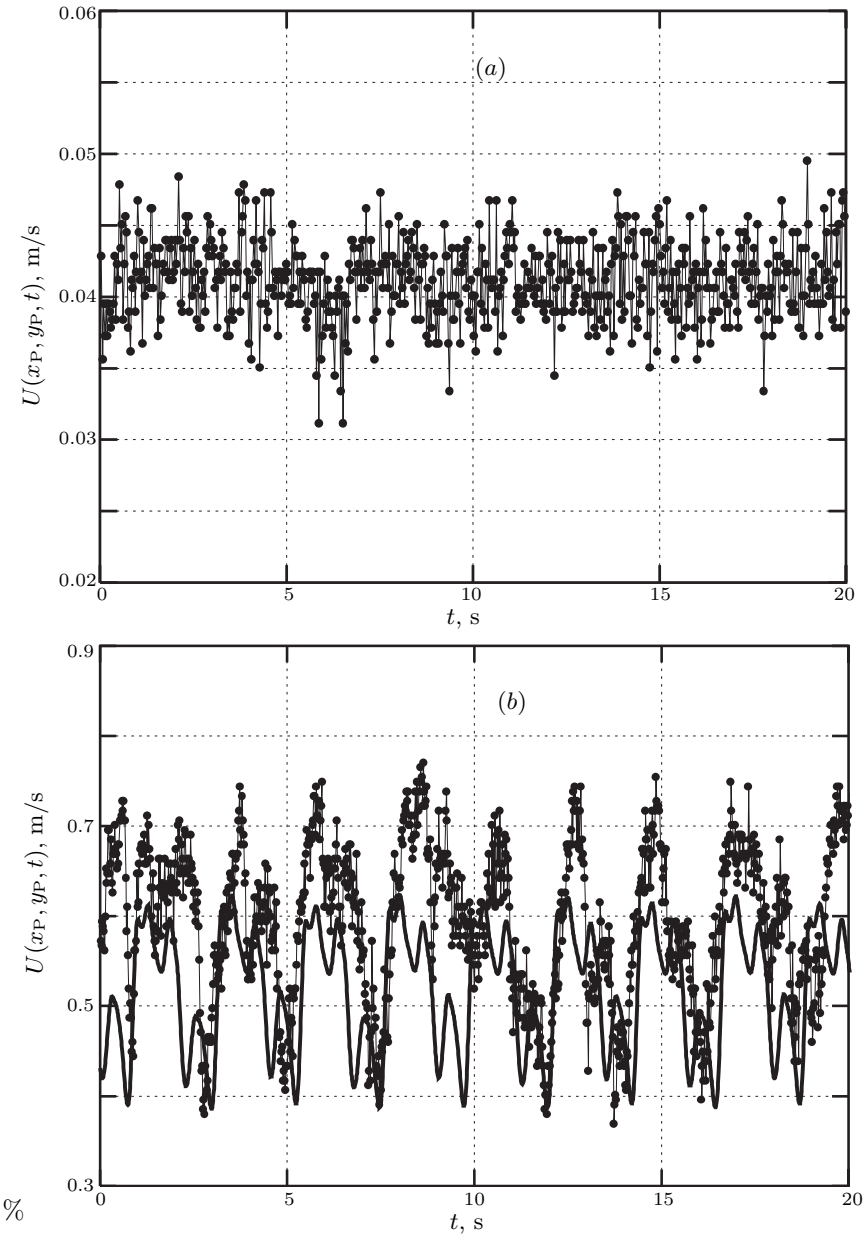

%

Fig. 7. Examples of measured velocity signals for type B flows. (*a*) $I_0 = 100$ A, (*b*) $I_0 = 1000$ A, solid line – calculated signal, dots – experiment.

Increasing the external current I_0 leads to higher velocities accompanied by a higher level of oscillations. Figure 7 gives typical measured velocity signals $U(x_P, y_P, t)$ as function of time. Whereas Fig. 7*a* shows for a rather low electrical current of $I_0 = 100$ A only some low-amplitude fluctuations, large-scale EVF oscillations can clearly be observed in the measured velocity signal at $I_0 = 1000$ A (type B) as shown in Fig. 7*b* where the numerically obtained velocity is added. It can be readily seen that the long-wave oscillations in the calculated signal $U(x_P, y_P, t)$ closely approximate those generated on the background of the short-wave oscillations in the experimental signal. The level of velocity fluctuations in those flows

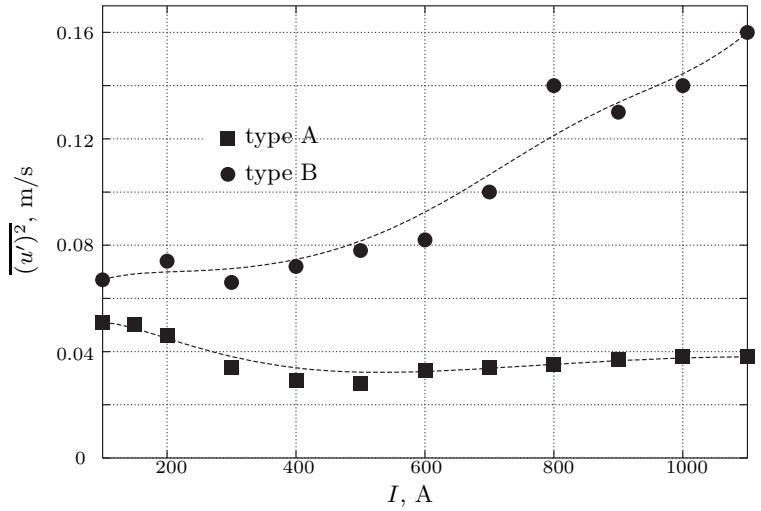

Fig. 8. Rms values of the measured velocity signals at the point (x_p, y_p) vs electrical current.

is illustrated in Fig. 8 which gives the dependence of the root-mean-square value $\overline{u'^2} = \sqrt{\sum_{i=1}^{N_t}(u'(t_i))^2/N_t}$ of the function $u'(t) = (U(x_\mathrm{P}, y_\mathrm{P}, t)/\overline{U}(x_\mathrm{P}, y_\mathrm{P}) - 1)$ on the electrical current. Whereas in case A this rms value remains almost constant for increasing current, it significantly increases in case B. It is interesting to note that the mean velocity $\overline{U}(x_\mathrm{P}, y_\mathrm{P})$ in case B is always smaller compared to case A, see Fig. 5. There is only one reason for this behaviour of the rms-values – the increase of EVF large-scale oscillation level in case B.

Figure 9 shows the energy $f_2 = \sum_k F_k^2$ of the signal $u'(t)$, where $F_k \equiv FT_k(u')$ is the Fourier-spectrum obtained by a standard Fourier-transform [15]. One can see that the level of oscillations for the EVF of type B is higher than for type A, however, for both EVF types, f_2 grows with the increase of the electric current. An explanation for the latter is that f_2 takes into account all fluctuations of the measured signal whereas the UDV measuring technique is known [14] to allow

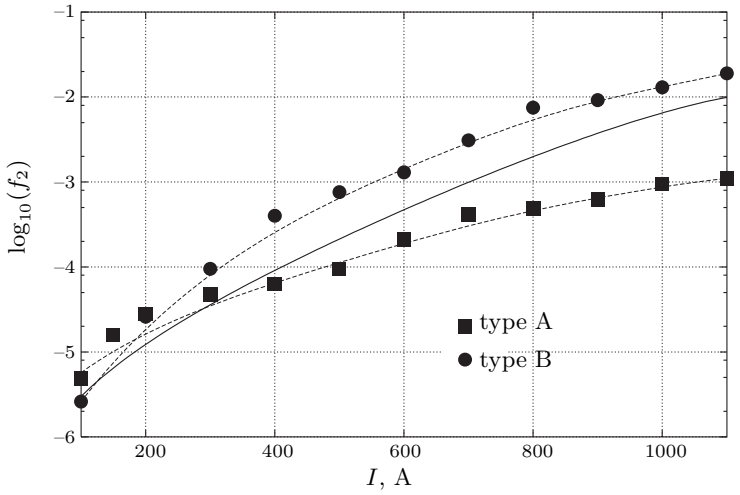

Fig. 9. Energy f_2 of the measured velocity signals at the point (x_p, y_p) vs electrical current: dots – experimental data for types A and B, solid line – calculations for type B.

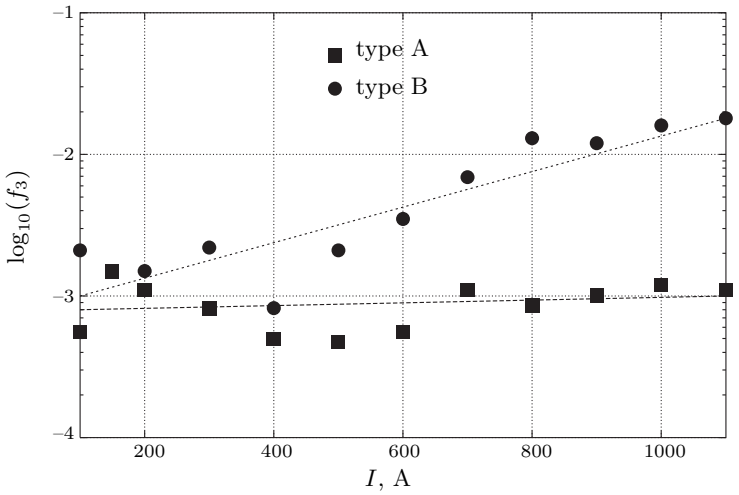

Fig. 10. Energy f_3 of the velocity profiles at $x = x_p$ vs electrical current.

only the resolution of a restricted bandwidth limited by the maximum achievable profile repetition rate, which typically is of the order of about 20 Hz. Thus, velocity oscillations of higher frequency cannot be resolved, but the obtained results confirm that UDV is well-suited for the measurement of the mean flow and its low-frequency oscillations. Along with the analysis of the fluctuating signals at one single point as in Figs. 8 and 9, it is also interesting to calculate the energy f_3 based on the velocity profile along the y-axis. The related Chebyshev spectrum is obtained following the standard procedure [15]

$$u^*(t) = TT_m(u'^*) = \frac{2}{C(m)M} \sum_{i=0}^{N_y} \frac{u'^*(y_i,t)\cos(m\pi y_i)}{C(i)}, \tag{7}$$

where $C(k) = 2$ for $k = 0$, $k = N_y$ and $C(k) = 1$ for the rest. We transformed the functions $u'^*(x_\mathrm{P}, y_i, t) \equiv U(x_\mathrm{P}, y_i, t)/ < U(x_\mathrm{P}\mathrm{P}, y_i, t) >$ which are the profiles divided by their coordinate-averaged value. Calculating for each external electrical current the energy f_3 via $f_3 = \sum_k G_k^2$ where $G_k = FT_k(u^*)$ leads to results shown in Fig. 10. As expected, the smoothing associated with the Chebyshev spectrum procedure eliminates the short-wave components and the results resemble the dependencies as obtained for the root-mean-square values in Fig. 8.

Fig. 11 shows the frequency spectra of a set of velocity measurements of type B flows. A clear peak at about 0.3 Hz is obtained at higher intensities of the mean velocity.

These results are an evident demonstration of the fact that in the present case the EVF with two-eddies is less stable than the EVF with one eddy. This behaviour corresponds well to the known effect that the higher the number of eddies the lower the system stability. In our investigation, besides the primary eddies (ψ_1 and ψ_2 in Fig. 1), small secondary eddies are initiated by the primary eddies in the corners of the layer (sketched as ψ_3 and ψ_4 in Fig. 1). A large-scale eddy (type A) is enclosed in the plane layer and, as the analysis of profiles showed, has no freedom to generate large and intensive secondary eddies. The EVF of type B demonstrates a very different situation. With the increasing electric current the eddies tend to press themselves to the vertical wall of the layer near the jumper of the C-core. At the same time, the couple of secondary eddies develops near the opposite vertical wall of the layer and their intensity increases. This tendency

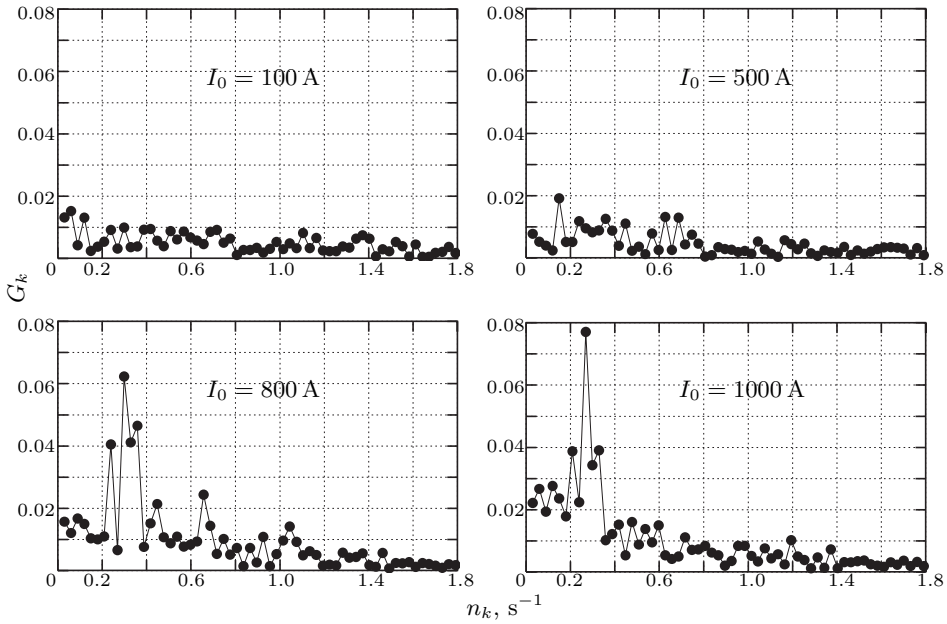

Fig. 11. Frequency spectra of type B flows for various electrical currents

can be assumed as the main ground for the observed large-scale oscillations of the velocity field. Thus, the system geometry and the position of the C-core significantly influence the flow field in the considered layer. A close agreement between the theoretical and experimental results has been obtained. Thus, the applied model has proved to be capable of providing reliable data for this class of flow problems.

Acknowledgements. The research described in this publication was made possible in part by Award No. YSF 2002-424 from the International Association for the promotion of cooperation with scientists from the New Independent States of the former Soviet Union (INTAS). Additional support by German "Deutsche Forschungsgemeinschaft" in the frame of Collaborative Research Centre SFB 609 is gratefully acknowledged. We are grateful to J. Hüller for preparation of the experiments as well as S. Eckert for his support with the ultrasonic measurements.

REFERENCES

[1] I. Kolesnichenko, S. Khripchenko. Surface instability of the plane layer of conducting liquid. *Magnetohydrodynamics*, vol. 39 (2003), no. 4, pp. 427–434.

[2] D. Lubimov, G. Putin, V. Tchernatinsky. About convective motions in the Hele–Shaw cell. *Dokl. Acad. Nauk USSR*, vol. 235 (1977), no. 3, pp. 554–556 *(in Russian).*

[3] V. Kolesnichenko, S. Khripchenko. Vortical motion of a liquid in a plane layer with a free surface. *Magnetohydrodynamics*, vol. 29 (1993), no. 2, pp. 170–174.

[4] I. Kolesnichenko, S. Khripchenko. Mathematical simulation of hydrodynamical processes in the centrifugal MHD pump. *Magnetohydrodynamics*, vol. 38 (2002), no. 4, pp. 39–46.

[5] S. Eckert, G. Gerbeth. Velocity measurements in liquid sodium by means of UDV. *Experiments in Fluids*, vol. 32 (2002), pp. 542–546.

[6] D. Brito, H.–C. Nataf, P. Cardin, J. Auber, J.–P. Masson. UDV in liquid gallium. *Experiments in Fluids*, vol. 31 (2001), pp. 653–663.

[7] M. Nowak. Wall shear stress measurement in a turbulent pipe flow using UDV. *Experiments in Fluids*, vol. 33 (2002), pp. 249–255.

[8] S. Denisov, V. Dolgih, S. Khripchenko. Electrovortex Flow in Flat Channel. In: *Proc. MTLM Int. Workshop* (Dresden, Germany, October 1999), pp. 291–295.

[9] V. Zymin, S. Khripchenko. Two-dimensional representation of the magnetohydrodynamic equations of flow in plane-parallel channels with ferromagnetic cores. *Magnetohydrodynamics*, vol. 15 (1979), no. 4, pp. 117–122.

[10] V. Kolesnichenko, S. Khripchenko. Experimental study of the vortical motion of a fluid in a plane closed cavity. *Magnetohydrodynamics*, vol. 25 (1989), no. 2, pp. 69–72.

[11] G. Branover, A. Tsinober. *Magnetohydrodynamics for incompressible fluids* (Nauka, Moscow, 1970) *(in Russian).*

[12] D.C. Wilcox. *Turbulence modeling for CFD* (DCW Industries, Inc. La Canada, California), 1993.

[13] R. Peire, T. Taylor. *Numerical methods for the problems of fluid mechanics* (Gidrometeoisdat, Leningrad, 1986) *(in Russian).*

[14] A. Cramer, C. Zhang, S. Eckert. Local flow structures in liquid metals measured by ultrasonic Doppler velocimetry. *Flow Meas. Instr.*, vol. 15 (2004), pp. 145-153.

[15] P. Frick. *Turbulence: models and approaches* (Institute of computing research, Moskow-Izhevsk, 2003) *(in Russian).*

Received 29.11.2004